Shock Waves (2021) 31:239–253
https://doi.org/10.1007/s00193-021-00999-8

ORIGINAL ARTICLE

Shock interactions in inviscid air and CO_2–N_2 flows in thermochemical non-equilibrium

C. Garbacz[1] · W. T. Maier[2] · J. B. Scoggins[3] · T. D. Economon[4] · T. Magin[5] · J. J. Alonso[2] · M. Fossati[1]

Received: 13 March 2020 / Revised: 26 January 2021 / Accepted: 9 February 2021 / Published online: 11 May 2021

Abstract
The present study aims at providing insights into shock wave interference patterns in gas flows when a mixture different than air is considered. High-energy non-equilibrium flows of air and CO_2–N_2 over a double-wedge geometry are studied numerically. The impact of freestream temperature on the non-equilibrium shock interaction patterns is investigated by simulating two different sets of freestream conditions. To this purpose, the SU2 solver has been extended to account for the conservation of chemical species as well as multiple energies and coupled to the Mutation++ library (Multicomponent Thermodynamic And Transport properties for IONized gases in C++) that provides all the necessary thermochemical properties of the mixture and chemical species. An analysis of the shock interference patterns is presented with respect to the existing taxonomy of interactions. A comparison between calorically perfect ideal gas and non-equilibrium simulations confirms that non-equilibrium effects greatly influence the shock interaction patterns. When thermochemical relaxation is considered, a type VI interaction is obtained for the CO_2-dominated flow, for both freestream temperatures of 300 K and 1000 K; for air, a type V six-shock interaction and a type VI interaction are obtained, respectively. We conclude that the increase in freestream temperature has a large impact on the shock interaction pattern of the air flow, whereas for the CO_2–N_2 flow the pattern does not change.

Keywords Non-equilibrium shock interaction · Inviscid hypersonic CO_2 flow

1 Introduction

Providing reliable predictions of shock interference phenomena is the key in the design of high-speed vehicles. Shock waves that are generated by the nose of the fuselage may interact with other shocks emanating from the different components of the vehicle, e.g., wings, inlet cowls, etc. The interaction between shock waves often leads to severe heating and pressure loads acting on the surfaces of the vehicle, affecting performance and airworthiness, and may impose additional thermal protection system requirements that increase the weight of the vehicle. The occurrence of shock wave interference can also be encountered in the flow path of the propulsion system of high-speed vehicles, where the flow is heated up before entering the system. At hypervelocity conditions, non-equilibrium physical processes such as finite-rate chemistry and internal energy exchange greatly influence the interaction mechanisms and the aerothermodynamic interactions with the surfaces of the vehicle. The problem of non-equilibrium shock interference has been widely studied in the literature, but due to its complexity and multi-physics nature, it is not yet fully understood. Most of the existing literature focuses on the Earth's atmosphere, thus only considering air and/or nitrogen flows. However, space missions to Mars have increased the need for better

Communicated by A. Sasoh.

✉ C. Garbacz
ana.gomes@strath.ac.uk

M. Fossati
marco.fossati@strath.ac.uk

[1] Aerospace Centre of Excellence, University of Strathclyde, Glasgow G1 1XJ, UK

[2] Stanford University, Stanford, CA 94305, USA

[3] École Polytechnique, Route de Saclay, 91128 Palaiseau, France

[4] SU2 Foundation, San Francisco, CA 94158, USA

[5] von Karman Institute for Fluid Dynamics, Rhode-Saint-Genese 1640, Belgium

understanding of carbon-dioxide-dominated atmospheres, for which the literature is scarce.

The first systematic study on shock interference mechanisms was carried out by Edney [1], who conducted experiments on the impingement of an oblique shock over a bow shock in front of a cylinder. By changing the location of this intersection, distinct shock interference patterns were identified and classified into six different shock interaction types using a classical shock-polar approach. The pioneering work of Edney was eventually adopted to classify shock interference patterns over other geometries such as the double-wedge case considered in this paper. The latter geometry is particularly relevant since it is found inside the propulsive systems of space vehicles. Furthermore, it represents regions in the proximity of control surfaces and/or the fuselage-canopy area. Inviscid flow over double wedges under the perfect gas assumption was numerically studied by Olejniczak et al. [2] in order to identify the shock interaction patterns resulting from increasing the angle of the second wedge. The transition between type VI and type V (transition types VI–V), as well as the six-shock and seven-shock configurations of type V, was investigated in more detail by Halder et al. [3]. Different possible configurations of the type V interaction, including the transition between a regular reflection and a Mach reflection (RR–MR transition), were numerically explored by Hu et al. [4] by changing the angle of the second wedge. Unsteady behaviour in flows over double wedges was first reported by Ben-Dor et al. [5]. Self-induced oscillations giving rise to extremely high pressure loads were found in the type V shock interaction pattern for a range of angles of the second wedge. The oscillatory wave patterns, associated with the interaction of shock waves with the slip layers emanating from the triple points, were investigated by Hu et al. [4].

In hypersonic flight conditions, temperatures tend to exceed the threshold for triggering real-gas effects, such as thermodynamic relaxation and chemical reactions. An accurate representation of such aerothermodynamic environments can therefore only be achieved by accounting for thermochemical non-equilibrium. Tchuen et al. [6,7] confirmed the necessity of re-analysing shock interactions with thermochemical non-equilibrium when hypersonic conditions are considered. By comparison with the perfect gas model, it was concluded that real-gas effects significantly influence the shock structure and the surface pressure. In the case of flow of air over a 15°–45° double-wedge configuration, it was observed that taking into account non-equilibrium effects caused the interaction pattern to change from a type V to a type VI interaction [6]. A similar tendency was found for a 15°–60° configuration, for which the shock layer thickness decreased significantly, even though the wave structure remained the same [7]. Focusing instead on the transition types VI–V, Li et al. [8] also studied the effects of using a real-gas model. It was found that the inclusion of non-equilibrium effects results in a delay of this transition, with respect to the critical value of the second-wedge angle.

Several other studies have focused exclusively on studying shock interactions by accounting for these effects [9–13]. Atkins and Deiterding [13] modelled thermochemical non-equilibrium in an accurate and robust way by coupling the Mutation++ thermochemistry library [14] (Multicomponent Thermodynamic And Transport properties for IONized gases in C++) to an adaptive mesh refinement solver. A double-wedge geometry with a type V interaction pattern was used as a test case to demonstrate the solver's ability to address non-equilibrium flow features in a highly resolved manner. The RR–MR transition in the type V interaction was studied in detail in Refs. [10–12], and, overall, it was concluded that the dominant cause for this transition is the migration and collision of the two triple points.

The previously mentioned studies do not extend into the CO_2 flows of interest in this work. CO_2 is a triatomic molecule showing a rather different behaviour from N_2 and O_2 molecules with respect to the energy redistribution among the internal degrees of freedom. This results in a characteristic vibrational temperature that is lower than in the case of air, with a non-negligible impact on the non-equilibrium processes. Using the two-temperature model developed for air with some extensions and modifications, Candler [15] studied a Martian atmospheric entry flow considering a CO_2–N_2 composition. Results showed that, due to the very fast vibrational relaxation of CO_2, there is very little thermal non-equilibrium. Additionally, at energies below the threshold for CO dissociation, the flow is nearly in chemical equilibrium and, at higher energies, CO dissociation leads to strong chemical non-equilibrium. The two-temperature non-equilibrium model for CO_2 was developed by Park [16]. The application to a re-entry simulation of a stagnation-line flow confirmed the conclusions drawn by Candler. In Ref. [17], it was shown that comparisons between the two-temperature model for CO_2 and the more detailed state-to-state approach showed a good agreement. Furthermore, validation work was carried out by Liao et al. [18] by comparing experimental measurements of shock stand-off distances over hypersonic spheres in a CO_2 flow to the corresponding numerical simulations. It was concluded that, under the studied conditions, the two-temperature model is applicable.

To the best of the authors' knowledge, the literature discussing the identification of shock wave interference patterns and the associated aerothermal loads in the case of CO_2-dominated flows is still not fully consolidated. Windisch et al. [19] simulated the intersection between an oblique shock and a bow shock in front of a cylinder with a CO_2-dominated flow and observed the type VII interaction. A comparison with the same test case but considering instead a N_2 mixture revealed that the post-shock temperatures were

significantly lower for the gas model of the Martian atmosphere, resulting in a higher fluid density and a much smaller shock stand-off distance. Moreover, thermal non-equilibrium was nearly non-existent, as expected. Recently, the authors have taken a first step to study shock interference patterns in CO_2 flows over double wedges [20]. It was shown that, for the simulated conditions, the shock patterns in CO_2 flows differ from the ones obtained for air. Likely due to the much faster vibrational relaxation of CO_2 molecules, lower temperatures and higher densities were obtained, which resulted in smaller shock angles and flow patterns that were more attached to the wall. Further work is required to understand shock interference phenomena in non-equilibrium flows primarily composed of CO_2. The purpose of the present study is to extend our previous work and conduct a systematic study where the impact of the freestream temperature is further assessed. Due to shock/boundary-layer interactions, viscous effects play a large role in this type of flows and can greatly influence the structure of the flow features [6,7]. The additional length scales introduced by a viscous model make the shock interaction analysis very difficult, and an inviscid model can be a good starting point for the fundamental study of shock interaction patterns with focus on the gas dynamics. Therefore, the non-equilibrium high-Mach-number inviscid flow over a double-wedge configuration is simulated with two different sets of freestream conditions. Shock interference patterns over double wedges when a CO_2-dominated flow is considered are evaluated and compared to the case of air. Furthermore, in order to better assess non-equilibrium effects, the same simulations are run with a calorically perfect ideal gas model.

The remainder of this paper is organized as follows. The governing equations are presented with emphasis on the physical modelling of finite-rate chemistry and thermal non-equilibrium. Solvers and numerical methods employed in this work are described, as well as validation tests. The computational analysis of flows over double wedges is presented, including a grid convergence study, a study of the shock interference patterns with changes in the freestream temperature and a comparison between different mixtures with a focus on the non-equilibrium effects. Finally, the main conclusions are summarized in the last section.

2 Physical and numerical models

2.1 Physical modelling and governing equations

The system of governing equations is obtained following classical approaches presented in the literature for an inviscid, chemically reacting, non-equilibrium flow [21]. The two-temperature model by Park [22] is used, where the translational energy mode is assumed to be at equilibrium with the rotational one, and the vibrational energy mode is assumed to be at equilibrium with the electronic one. In a compact form, the system can be described as

$$\frac{\partial \mathbf{U}}{\partial t} + \nabla \cdot \mathbf{F}(\mathbf{U}) = \mathbf{Q}(\mathbf{U}), \tag{1}$$

where the vectors of conservative variables, convective fluxes, and source terms are given by

$$\mathbf{U} = \begin{Bmatrix} \rho_1 \\ \vdots \\ \rho_{n_s} \\ \rho \mathbf{u} \\ \rho e \\ \rho e^{\mathrm{ve}} \end{Bmatrix}, \quad \mathbf{F} = \begin{Bmatrix} \rho_1 \mathbf{u} \\ \vdots \\ \rho_{n_s} \mathbf{u} \\ \rho \mathbf{u} \otimes \mathbf{u} + p\bar{I} \\ \rho \mathbf{u} h \\ \rho \mathbf{u} e^{\mathrm{ve}} \end{Bmatrix}, \quad \mathbf{Q} = \begin{Bmatrix} \dot{\omega}_1 \\ \vdots \\ \dot{\omega}_{n_s} \\ 0 \\ 0 \\ \dot{\Omega} \end{Bmatrix}, \tag{2}$$

and $\mathbf{u}$ is the flow velocity vector, ρ is the density of the mixture, ρ_s is the density of species s, p is the static pressure, e and e^{ve} are, respectively, the total energy per unit mass and the vibrational energy per unit mass for the mixture, h is the total enthalpy per unit mass, $\dot{\omega}_s$ is the chemical source energy of species s, index s denotes the sth chemical species, and n_s is the total number of species.

Calculating the non-equilibrium thermodynamic state and source terms is necessary to close the system of governing equations that describes hypersonic flows. This is achieved by means of coupling with appropriate multi-temperature thermochemistry models. The equations presented below describe the implementation of the two-temperature model for a mixture composed of neutral species, provided by the Mutation++ library [14]. Each individual species s is assumed to behave as an ideal gas. Hence, the total pressure of the mixture p is defined by Dalton's Law as the summation of the partial pressures associated with each species p_s, determined by the ideal gas law,

$$p = \sum_{s=1}^{n_s} p_s = \sum_{s=1}^{n_s} \rho_s \frac{R_u}{M_s} T_{tr}, \tag{3}$$

where R_u is the universal gas constant, M_s is the molar mass of species s, and T_{tr} is the trans-rotational temperature. The total specific energy of the flow e is given as the sum of the internal and kinetic energies:

$$e = \sum_{s=1}^{n_s} c_s e_s + \frac{1}{2} u^2, \tag{4}$$

where c_s is the mass fraction of species s, u is the magnitude of the flow velocity vector, and e_s is the specific internal energy of the species, given by the sum of the energy

of formation and the contribution of each internal mode (t-translational, r-rotational, v-vibrational, e-electronic),

$$e_s = e_s^{\mathrm{t}}\left(T_{\mathrm{tr}}\right) + e_s^{\mathrm{r}}\left(T_{\mathrm{tr}}\right) + e_s^{\mathrm{v}}\left(T_{\mathrm{ve}}\right) + e_s^{\mathrm{e}}\left(T_{\mathrm{ve}}\right) + e_s^{0}. \tag{5}$$

Using a combination of statistical thermodynamics and quantum mechanics, the internal mode energies are defined on the basis of the rigid-rotor harmonic oscillator model (RRHO) as:

$$e_s^{\mathrm{t}}\left(T_{\mathrm{tr}}\right) = \frac{3}{2}\frac{R_{\mathrm{u}}}{M_s}T_{\mathrm{tr}}, \tag{6}$$

$$e_s^{\mathrm{r}}\left(T_{\mathrm{tr}}\right) = \begin{cases} \frac{R_{\mathrm{u}}}{M_s}T_{\mathrm{tr}}, & \text{for linear molecules,} \\ 0, & \text{for atoms,} \end{cases} \tag{7}$$

$$e_s^{\mathrm{v}}\left(T_{\mathrm{ve}}\right) = \begin{cases} \frac{R_{\mathrm{u}}}{M_s}\sum_v \frac{\theta_{v,s}^{\mathrm{v}}}{\exp\left(\theta_{v,s}^{\mathrm{v}}/T_{\mathrm{ve}}\right)-1}, & \text{for molecules,} \\ 0, & \text{for atoms,} \end{cases} \tag{8}$$

$$e_s^{\mathrm{e}}\left(T_{\mathrm{ve}}\right) = \frac{R_{\mathrm{u}}}{M_s}\frac{\sum_i g_{i,s}\theta_{i,s}^{\mathrm{e}}\exp\left(-\theta_{i,s}^{\mathrm{e}}/T_{\mathrm{ve}}\right)}{\sum_i g_{i,s}\exp\left(-\theta_{i,s}^{\mathrm{e}}/T_{\mathrm{ve}}\right)}, \tag{9}$$

where $\theta_{v,s}^{\mathrm{v}}$ is the characteristic vibrational temperature of species s and vibrational mode v, $g_{i,s}$ and $\theta_{i,s}^{\mathrm{e}}$ are the degeneracy and characteristic electronic temperature, respectively, at energy level i for species s. The formation energy e_s^0 is referenced at the standard state conditions of 298.15 K and 1 atm.

The conservation equation for the mass of the mixture is replaced by a mass conservation equation for each species in the gas, incorporating a production/destruction term that results from chemical activity. The chemical source term $\dot{\omega}_s$ is given by

$$\dot{\omega}_s = M_s\sum_{r=1}^{n_{\mathrm{r}}}\left(\nu_{s,r}'' - \nu_{s,r}'\right)\left[k_{\mathrm{f},r}\prod_{j=1}^{n_{\mathrm{s}}}\hat{\rho}_j^{\nu_{j,r}'} - k_{\mathrm{b},r}\prod_{j=1}^{n_{\mathrm{s}}}\hat{\rho}_j^{\nu_{j,r}''}\right], \tag{10}$$

where n_{r} and n_{s} are, respectively, the number of reactions and the number of species, ν_s' is the forward reaction stoichiometry coefficient, ν_s'' is the backward reaction stoichiometry coefficient, $\hat{\rho}_j$ is the molar density, $k_{\mathrm{f},r}$ is the forward reaction rate, and $k_{\mathrm{b},r}$ is the backward reaction rate. The forward reaction rate for each reaction r is defined according to the modified Arrhenius equation

$$k_{\mathrm{f},r} = A_r T_{\mathrm{c}}^{N_r}\exp\left(-\frac{\theta_r}{T_{\mathrm{c}}}\right), \tag{11}$$

where the coefficients A_r, θ_r, and N_r are obtained from experimental data and are, respectively, the reaction rate constant, the activation temperature, and an exponent. The backward reaction rates $k_{\mathrm{b},r}$ are determined from the equilibrium reaction rates, $k_{\mathrm{b},r} = k_{\mathrm{f},r}/k_{\mathrm{eq},r}$ for every reaction r. The equilibrium reaction rates $k_{\mathrm{eq},r}$ are determined as a function of the Gibbs free energy. The temperature T_{c} is the controlling temperature determined by Park's two-temperature model [22]:

- Dissociation reactions $\mathrm{AB} + \mathrm{M} \rightleftharpoons \mathrm{A} + \mathrm{B} + \mathrm{M}$

  $T_{\mathrm{c}} = \sqrt{T_{\mathrm{tr}}T_{\mathrm{ve}}}$ for the forward rate; $T_{\mathrm{c}} = T_{\mathrm{tr}}$ for the backward rate;
- Exchange reactions $\mathrm{AB} + \mathrm{C} \rightleftharpoons \mathrm{A} + \mathrm{BC}$

  $T_{\mathrm{c}} = T_{\mathrm{tr}}$.

In the two-temperature model, the energy transfer mechanisms, that determine the change in vibrational energy of the mixture, are accounted for in the source term vector. The source term $\dot{\Omega}$ is defined as the sum of the vibrational-to-translational energy transfer and energy exchanges due to chemical activity,

$$\dot{\Omega} = \sum_{s=1}^{n_{\mathrm{s}}}\dot{\Omega}_s^{\text{t-r:v-e}} + \dot{\Omega}_s^{\text{c:v}} + \dot{\Omega}_s^{\text{c:e}}. \tag{12}$$

The term $\dot{\Omega}^{\text{t-r:v-e}}$ concerns the rate of energy exchange between the translational and vibrational energy modes, following the Landau–Teller model [23]

$$\dot{\Omega}_s^{\text{t-r:v-e}} = \rho_s\frac{e_s^{\mathrm{v}}(T) - e_s^{\mathrm{v}}\left(T_{\mathrm{v}}\right)}{\tau_s^{\text{V-T}}}. \tag{13}$$

The vibrational relaxation time of each species, $\tau_s^{\text{V-T}}$, is given by the Millikan and White empirical formula [24] and the Park correction [22],

$$\tau_s^{\text{V-T}} = \tau_s^{\text{MW}} + \tau_s^{\text{P}}, \tag{14}$$

where τ_s^{MW}, the Millikan and White relaxation time of species s, depends on the vibrational relaxation times of the interactions with collision partners r and the corresponding molar fractions X_r, as follows:

$$\tau_s^{\text{MW}} = \left(\sum_{r=1}^{n_{\mathrm{s}}}\frac{X_r}{\tau_{s-r}^{\text{MW}}}\right)^{-1}, \tag{15}$$

$$\tau_{s-r}^{\text{MW}} = \exp\left(A_{s,r}\left(T^{-\frac{1}{3}} - B_{s,r}\right) - 18.42\right)\left(\frac{p}{101325}\right)^{-1}\ [\mathrm{s}]. \tag{16}$$

The Park correction is given by

$$\tau_s^{\text{P}} = \left(N_s\sigma_s\sqrt{\frac{8R_{\mathrm{u}}T_{\mathrm{tr}}}{\pi M_s}}\right)^{-1}, \tag{17}$$

where r denotes the rth species, X_r is the molar fraction, N_s is the number density, and σ_s is an effective cross section for vibrational relaxation. The change in vibrational-electronic energy of the mixture due to the production/destruction of species is accounted for in the terms $\dot{\Omega}_s^{\text{c:v}}$ and $\dot{\Omega}_s^{\text{c:e}}$, given by

$$\dot{\Omega}_s^{\text{c:v}} = c_1 \dot{\omega}_s e_s^{\text{v}}, \qquad \dot{\Omega}_s^{\text{c:e}} = \dot{\omega}_s e_s^{\text{e}}. \tag{18}$$

The coupling between vibrational energy modes and finite-rate chemistry follows a simple non-preferential dissociation model, for which it is assumed that molecules are destroyed or created at the average vibrational energy of the cell; therefore, $c_1 = 1$.

2.2 Solvers and numerical methods

The open-source SU2 software[1] suite [25] written in C++ and Python is the basis for this study. It is built specifically for the analysis of partial differential equations (PDEs) and PDE-constrained optimization problems on unstructured meshes with the state-of-the-art numerical methods. The solver is rapidly establishing itself within the open-source community as a prominent software for multi-physics analysis and design, including the simulation of chemically reactive and non-equilibrium flows [20,26] with the development of SU2-NEMO (Non-Equilibrium MOdels solver). The approach adopted for numerical discretization is based on classical literature on the subject. A finite-volume edge-based formulation is used with the AUSM scheme [27] (advection upstream splitting method) together with MUSCL (monotonic upstream-centred scheme for conservation laws) and standard limiting procedures. A dual time-stepping approach with a second-order backward-difference discretization of the time derivative terms is adopted to address unsteadiness.

The closure of the governing equations for the system of interest is achieved by means of coupling with appropriate thermochemistry models (presented in Sect. 2.1). In this regard, the implementation in the present work extended SU2-NEMO by linking to the Mutation++ library[2] [14] that provides efficient algorithms for the computation of thermodynamic, transport (viscosity, thermal conductivity, and diffusion) and chemical kinetic gas properties. The library has been designed for robustness over a wide range of temperatures and its accuracy in dealing with multi-temperature models, with the following constraints in mind: (1) high fidelity of the physical models, ensuring that the laws of thermodynamics are satisfied and that results are validated against the existing experimental data, (2) low computational cost, (3) a modern, object-oriented, extensible framework, and (4) detailed in-source and user's guide documentation in order to facilitate model improvement and collaboration.

2.3 Validation of thermochemical non-equilibrium models

Both the SU2 software and the Mutation++ library have been extensively validated [14,25]. To validate the additional numerical implementation that concerns the link between these two codes, the canonical problem of a zero-dimensional adiabatic heat bath was chosen. This type of test case allows to isolate the vibrational-to-translational energy transfer together with vibration-chemistry coupling from the CFD (computational fluid dynamics) simulation, with the purpose of validating the thermochemical relaxation process.

The case of heat bath with a chemically reacting mixture of standard five-species air (N_2, O_2, N, O, and NO) in thermal non-equilibrium was tested. The initial number density is set to 10^{25} m^3/s with molar fractions N_2: 0.79 and O_2: 0.21. The initial translational and vibrational temperatures are 15,000 K and 300 K, respectively. The mechanism of reaction is taken from Park [28,29], and a non-preferential model is considered. A time step of 1.0×10^{-10} s is used in the simulation. Figure 1 shows the evolution of (a) translational and vibrational temperatures and (b) species molar fractions with time. Results obtained with SU2-NEMO are compared with the ones provided by another hypersonic CFD code, the Michigan Aerothermal Navier–Stokes Solver LeMANS [30]. A fair agreement is obtained between the two different codes. A perfect match is obtained for the equilibrium temperatures and molar fractions, whereas a 3% discrepancy of vibrational temperature is observed at its peak value, approximately for the same instant of time at which the largest discrepancies of molar fractions are observed. As expected from a non-preferential dissociation model that is used in both solvers, the maximum in vibrational temperature occurs at an instant of time where $T_{\text{tr}} = T_{\text{ve}}$. This model assumes that the molecules are destroyed or created at the average vibrational energy of the cell, which causes the vibrational-to-translational energy transfer to govern the thermochemical relaxation process. Mathematically, the vibration-chemistry coupling term $\dot{\Omega}^{\text{c:v-e}}$ is much smaller than the term $\dot{\Omega}^{\text{t-r:v-e}}$ provided by the Landau–Teller model, for which $\frac{\mathrm{d}T_{\text{ve}}}{\mathrm{d}t} = 0$ at the same time that $T_{\text{tr}} = T_{\text{ve}}$. The slight discrepancies also are expected, since there are some differences in the modelling, namely Arrhenius law coefficients in the reaction mechanism as well as different thermodynamic database and handling of the electronic excitation.

[1] https://github.com/su2code/SU2.

[2] https://github.com/mutationpp/Mutationpp.

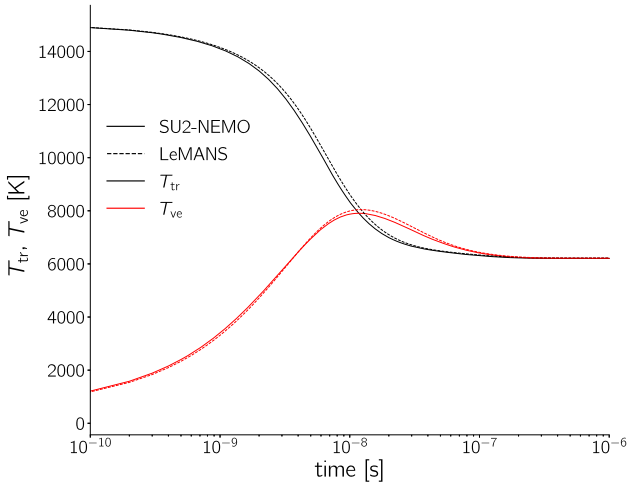

(a) Translational and vibrational temperatures.

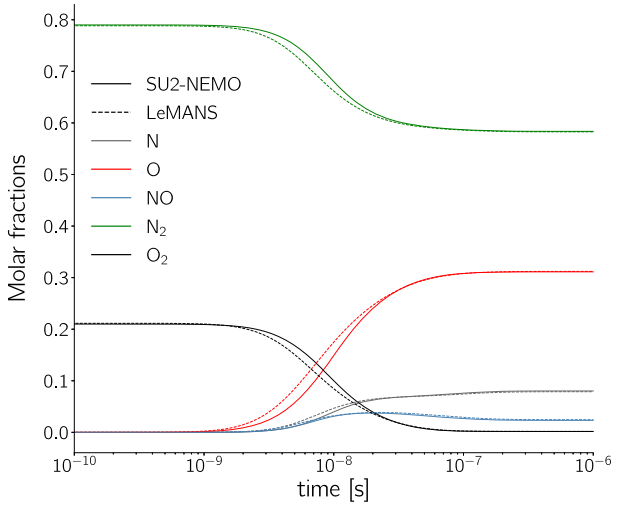

(b) Species molar fractions.

Fig. 1 Adiabatic thermal bath simulation for an air five-species mixture. Code-to-code comparison between SU2-NEMO and LeMANS

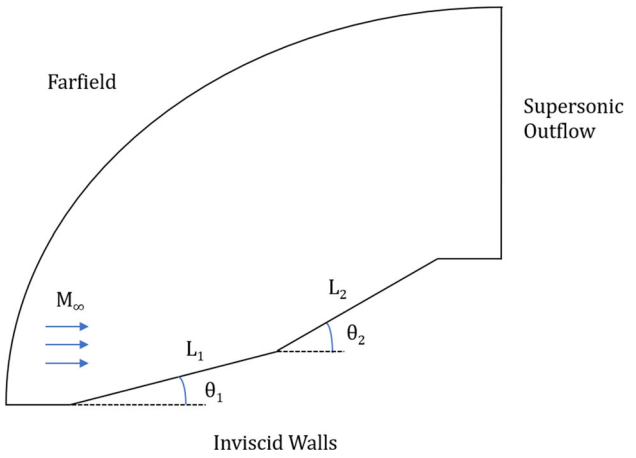

Fig. 2 Double-wedge geometry, computational domain, and boundary conditions

3 Computational analysis

In this section, shock interaction patterns in non-equilibrium flows over double-wedge geometries are discussed for different mixtures and values of the freestream temperature. For the flow of air, a mixture with five species (N_2, O_2, N, O, and NO) is considered, and the reaction mechanism is taken from the widely used references of Park [28,29]. For the CO_2–N_2 flow, a mixture with 10 species (C, N, O, C_2, N_2, O_2, CN, CO, NO, and CO_2) is used, and the reaction mechanism is taken from [16]. Following the approach of Candler [15], only CO_2 and N_2 are considered as initial species. At the conditions studied, ionization is assumed not to be important for the flow features.

The geometry and computational domain used in the study are illustrated in Fig. 2. Both wedges have the same length, i.e., $L_1/L_2 = 1$. The first wedge has an angle of $\theta_1 = 15°$, and the second wedge has an angle of $\theta_2 = 45°$. An inviscid wall boundary condition is imposed along the walls, supersonic outflow is used at the exit, and a farfield boundary condition is imposed at the remaining boundary. The freestream conditions are summarized in Table 1. For all simulations, the freestream Mach number and pressure are, respectively, $M_\infty = 9$ and $p_\infty = 390$ Pa. The initial mass fractions are $Y_{N_2} = 0.77$ and $Y_{O_2} = 0.23$ for air and $Y_{CO_2} = 0.95$ and $Y_{N_2} = 0.05$ for the CO_2–N_2 flow. It is assumed that the freestream flow is in thermal equilibrium, $T_{tr,\infty} = T_{ve,\infty} = T_\infty$. Two different values of freestream temperature are simulated: $T_\infty = 300$ K and $T_\infty = 1000$ K. The first case aims at simulating the occurrence of shock wave interference in a situation typical of external aerodynamics, in the proximity of control surfaces and/or the fuselage-canopy area, where the flow has been previously heated up by the vehicle nose shock. The higher value of freestream temperature simulates the interference phenomena in the case of internal aerodynamics of a propulsive system, for which the flow undergoes a series of shock waves before entering the system. To better understand the impact of non-equilibrium effects in this study, these simulations were also run using a calorically perfect ideal gas model—with $\gamma = 1.4$ for air and $\gamma = 1.29$ for the CO_2–N_2 mixture. Under the calorically perfect ideal gas assumption, the type of interaction that occurs depends only on the relevant non-dimensional parameters (which for inviscid flow are freestream Mach number M_∞, wedge length ratio L_1/L_2, specific heat ratio γ, wedge angles θ_1 and θ_2) [2], and therefore, only one value of freestream temperature was used, $T_\infty = 300$ K. The next three subsections present: Sect. 3.1 a grid independence study, Sect. 3.2 numerical results for air

Table 1 Simulation parameters

	M_∞	p_∞ [Pa]	T_∞ [K]	Mass fractions
Air	9	390	300/1000	N_2: 0.77
				O_2: 0.23
CO_2–N_2	9	390	300/1000	CO_2: 0.95
				N_2: 0.05

and CO_2–N_2 flows, and Sect. 3.3 the discussion of the results with respect to the non-equilibrium effects and its impact on the shock interaction patterns.

3.1 Grid independence

Shock interactions result in complex flow structures that can only be accurately captured using very fine grids. In order to avoid the consequent excessive computational times, adaptive mesh refinement is employed in this work, so that mesh resolution is increased only where it is needed. The baseline two-dimensional grid is an unstructured mesh composed only of triangular elements. Nodes are clustered near the walls and in the region where the interaction is expected to occur. Figure 3 shows the grid independence study for the case of an air five-species mixture with $T_{\mathrm{tr},\infty} = T_{\mathrm{ve},\infty} = 1000$ K. Results show the effects of different grid sizes on the (a) normalized surface pressure profile as well as (b), (c) normalized translational and vibrational temperatures, respectively, as a function of the normal distance from the wall δ, at a position on the surface of the second wedge where the most complex flow features are observed. For the scope of this paper, it is considered that grid convergence is achieved, since the discrepancies observed between the two most refined meshes are very small and they have no impact in the flow features associated with different shock patterns. A similar approach is used for all the different cases. For each one of the cases, the most refined grid is chosen. Table 2 shows the characteristic cell size (normalized by the length of the wedge) of the grids that are used in the numerical study. For each grid, the cell size is measured at two different locations of interest for the shock pattern, indicated, later in the paper, in Figs. 4 and 7: (1) shock wave and (2) contact discontinuity

3.2 Shock interaction patterns

In the first set of test cases, a mixture of air five species is considered. Figure 4 shows the normalized pressure and a numerical schlieren of the flowfield, and Fig. 5 shows translational and vibrational temperatures. Using a calorically perfect ideal gas model, a type V interaction with a nine-shock configuration is obtained. The schematic provided in Fig. 6a is used to analyse the pattern obtained numerically.

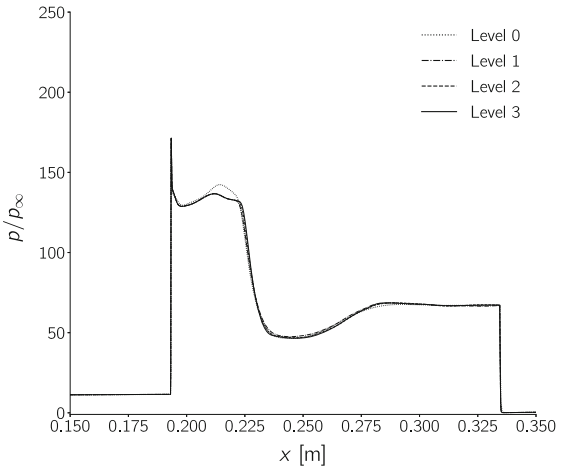

(a) Normalized surface pressure profile.

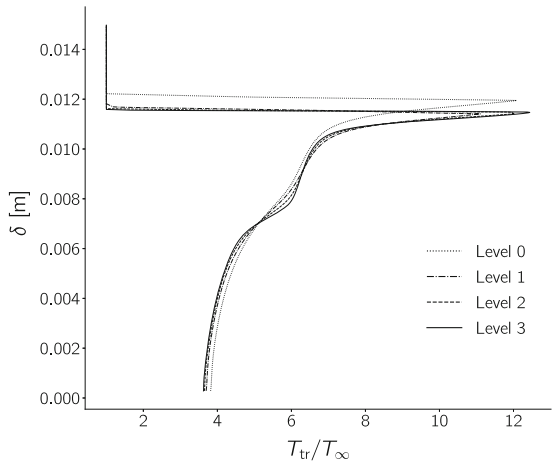

(b) Normalized translational temperature.

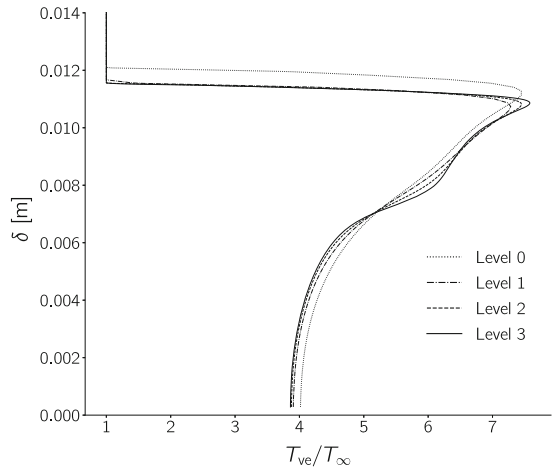

(c) Normalized vibrational temperature.

Fig. 3 Grid convergence study for the case of an air five-species mixture with $T_\infty = 1000$ K

Table 2 Characteristic cell size and number of nodes of final grids (locations 1 and 2 indicated in Figs. 4 and 7)

	Air			CO_2–N_2		
	Location 1	Location 2	Nodes	Location 1	Location 2	Nodes
$T_\infty = 300$ K	1.6×10^{-4}	3.8×10^{-4}	2,093,114	1.8×10^{-4}	1.9×10^{-4}	1,426,274
$T_\infty = 1000$ K	2.1×10^{-4}	2.2×10^{-4}	1,312,152	1.8×10^{-4}	1.9×10^{-4}	1,639,684

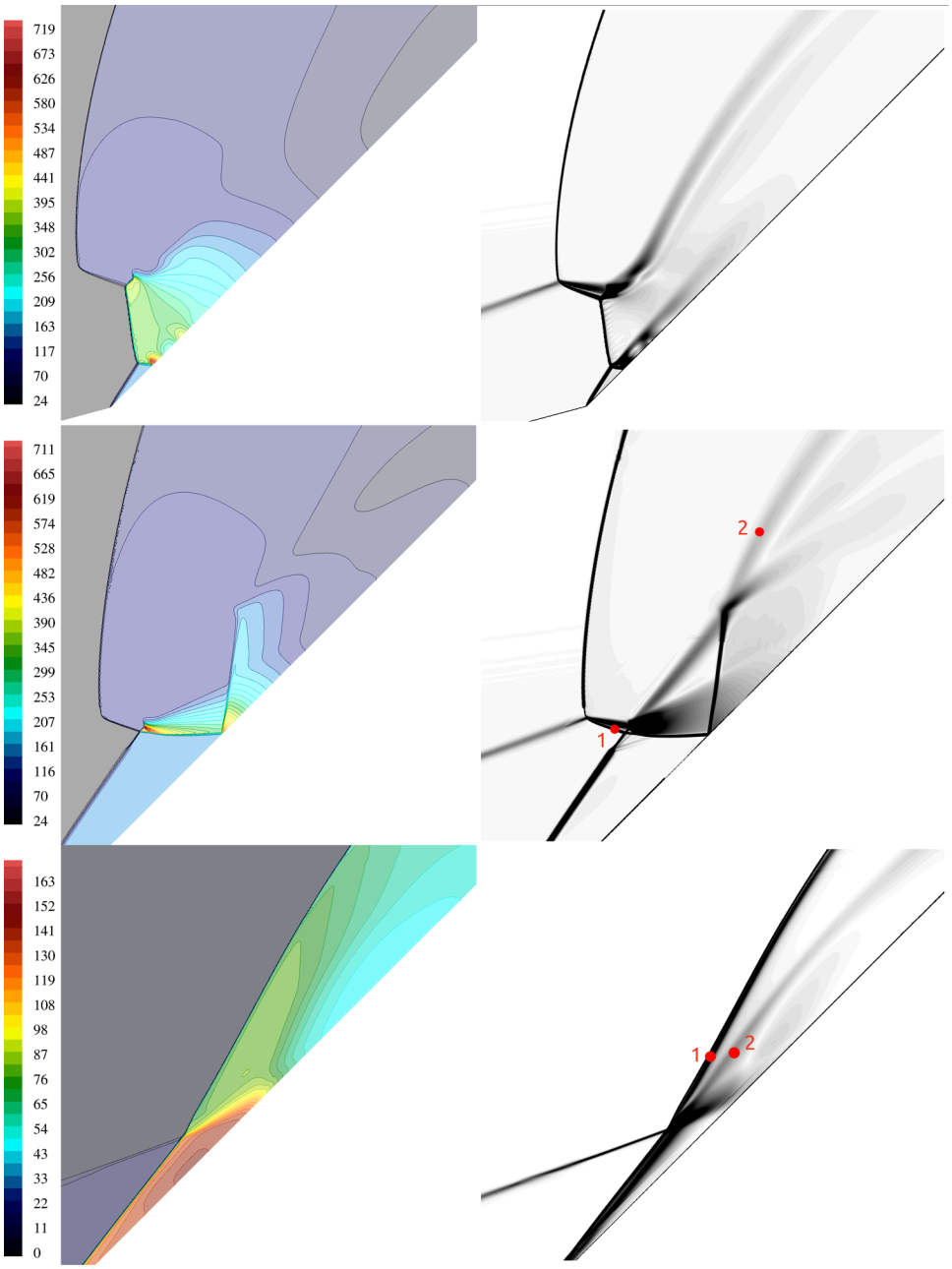

Fig. 4 Air flow over 15°–45° double wedge. Normalized pressure p/p_∞ (left), numerical schlieren (right); from top to bottom: calorically perfect ideal gas, non-equilibrium with $T_\infty = 300$ K, $T_\infty = 1000$ K

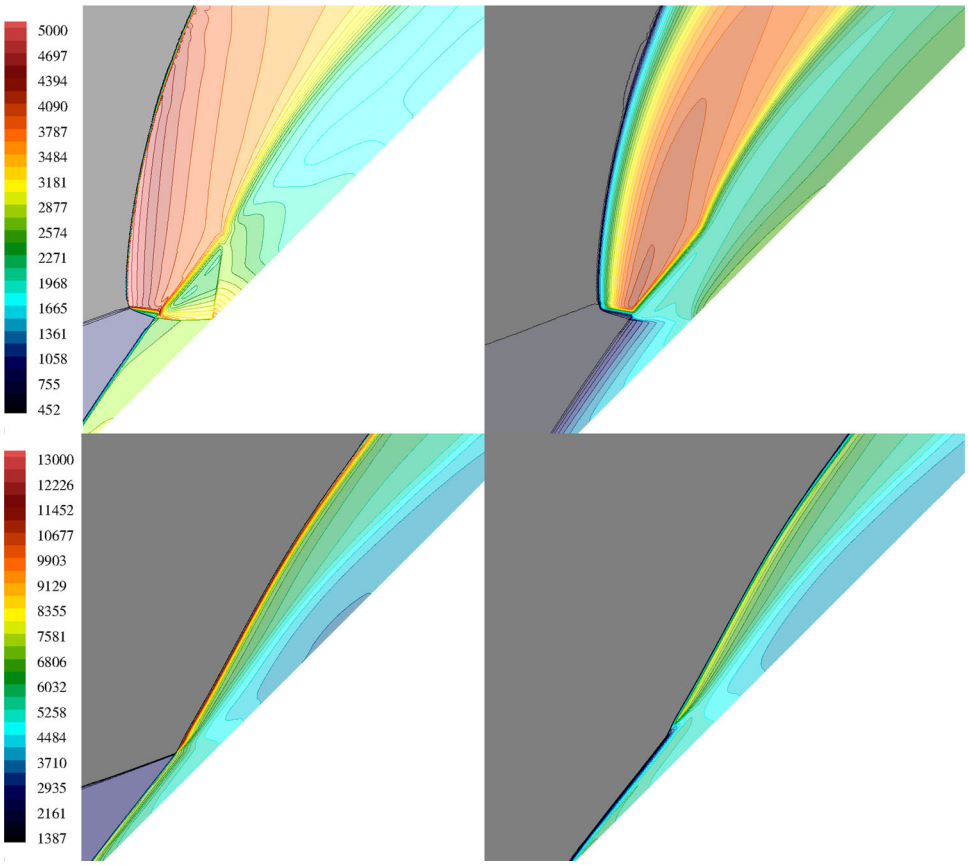

Fig. 5 Air flow over 15°–45° double wedge. Translational temperature T_{tr} (left), vibrational temperature T_{ve} (right); from top to bottom: non-equilibrium with $T_\infty = 300$ K, $T_\infty = 1000$ K

This interaction is characterized by four triple points. The upper triple point UTP is the intersection between the first oblique shock, the bow shock, and the transmitted shock SW3. The interaction of shock SW3 and the oblique shock generated in the corner between the two wedges—shock SW2—results in a Mach reflection denoted by MS2, which gives rise to the mid-triple point MTP (connecting SW3, MS2, and SW4). The lower triple point LTP concerns what is usually described as a lambda shock interaction, connecting MS2, the oblique shock from the corner between the two wedges SW2 and shock SW5. For the given freestream conditions and geometry, the flow is not able to meet both pressure equilibrium and flow tangency constraints with an incident and a reflected shock at the wall, which results in the reflection of shock SW5 on the surface of the second wedge as a normal shock in a second Mach reflection, giving rise to shock SW6 and the wall triple point WTP. From the upper and mid-triple points, UTP and MTP, respectively, two slip layers, SL1 and SL2 are emitted, bounding a thick contact surface. Furthermore, a third slip layer SL3 is emitted from the lower triple point LTP. Just behind the Mach reflection between the mid-triple and lower triple points, MTP and LTP, respectively, slip layers SL2 and SL3 assemble a converging stream tube. Shock SW4 is reflected on the slip layer SL1 as an expansion wave, turning the slip layer SL1 upward. Further downstream, this expansion wave impinges on the slip layer SL2, which is turned upward and lets the stream tube bounded by SL2 and SL3 diverge. This converging–diverging stream tube is a typical feature of the type V nine-shock configuration. The reflection of shock SW6 on the slip layer SL3 emits an expansion wave that makes SL3 turn upward. The flow between this contact discontinuity and the surface of the second wedge then undergoes a series of alternating isentropic compression and expansion waves, behaving as an underexpanded jet with regard to the adjacent flow region.

For a freestream temperature of $T_\infty = 300$ K, a type V interaction with a six-shock configuration is obtained. The type V interaction is characterized by one triple point P, as shown in the schematic illustrated in Fig. 6b. Point P is where the nose shock and the bow shock intersect, from which a transmitted shock PT emerges in a Mach reflection structure. The latter shock interacts with the oblique shock generated by the corner between the two wedges (shock TB), causing shock PT to reflect as shock TU (dark blue to red regions in the normalized pressure plot shown in Fig. 4) and shock TB to reflect as shock TR (light blue to yellow/green regions in the normalized pressure plot shown in Fig. 4) in a regular reflection structure. The resulting peak in surface pressure can be identified in Fig. 9. The reflection of these two shocks from opposite families is one of the key features in the type

V six-shock interaction. Downstream of the corner between the two wedges, shock TR undergoes a regular reflection on the surface of the second wedge and gives rise to shock RQ that can be observed in the pressure contours in the transition from light blue to green/yellow, in Fig. 4. Furthermore, a slip layer—evident in the temperature plots shown in Fig. 5—emanates from the triple point P. Shock TU reflects on the slip layer as an expansion wave that, in turn, merges with the reflected shock RQ, which further downstream is reflected by the slip layer as an expansion wave. The two expansion fans can be seen in the normalized pressure plots, where the contours change from yellow to green, light blue, and dark blue.

As the freestream temperature is raised to $T_\infty = 1000$ K, the shock interaction pattern completely changes and a type VI interaction is obtained, with a schematic shown in Fig. 6c. In this type of interaction, the flow is purely supersonic and oblique shock waves originating in the two corners directly intersect in point P, resulting in the appearance of a contact discontinuity that separates the flow that has passed through both shocks from the one that has passed through the second shock BP only. An expansion fan is emitted from the oblique shock intersection and reflected on the surface of the second wedge (transition of contours from red to green and blue). Some of the reflected expansion waves are deflected as they cross the slip layer and intersect with the oblique shock PS, weakening it. The remaining expansion waves are instead reflected by the contact discontinuity as compression waves, recompressing the fluid along the surface of the second wedge (closed light blue pressure contours).

In the second set of test cases, a mixture with CO_2, N_2, and eight other species is considered (C, N, O, C_2, N_2, O_2, CN, CO, NO, and CO_2). Figures 7 and 8 show the shock interaction patterns obtained for this mixture. In this case, except for the non-equilibrium simulation with $T_\infty = 1000$ K, the patterns obtained numerically are very different from the case of air. For the case of a calorically perfect ideal gas, a type V with a six-shock configuration is obtained. A description of this type of interaction has already been given for the case of non-equilibrium air with $T_\infty = 300$ K. A supersonic type VI—for which the wave structure has already been described for the case of non-equilibrium air with $T_\infty = 1000$ K—is obtained for $T_\infty = 300$ K and $T_\infty = 1000$ K. The differences in flow features observed between these three cases are relatively small. The shock angles differ slightly, and the interaction pattern is more attached to the wall as the freestream temperature is increased from 300 K to 1000 K in the case of CO_2. These differences can be quantitatively identified in terms of normalized surface pressure in Fig. 9. Despite the disparities in surface pressure just behind the corner shock wave, there is no impact on the shock interaction pattern. The effect of

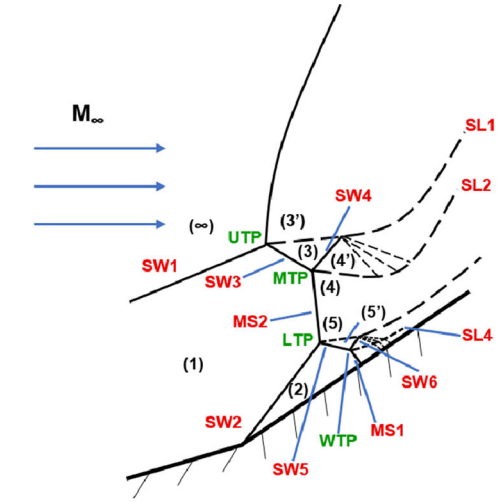

(a) Nine-shock type V interaction [10].

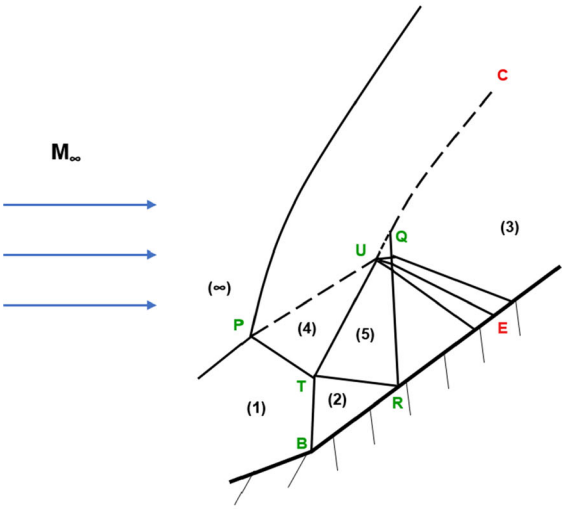

(b) Six-shock type V interaction [9].

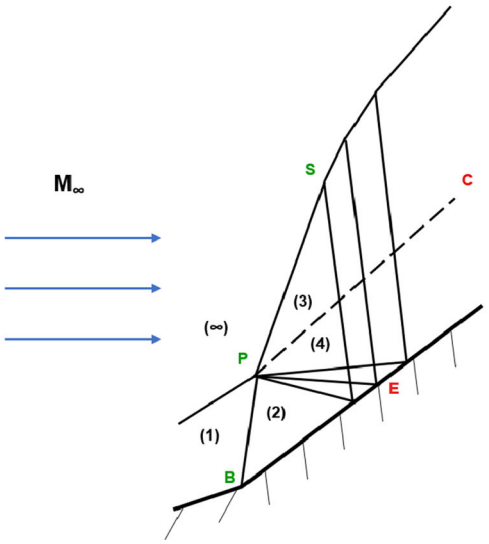

(c) Type VI interaction [9].

Fig. 6 Schematics of shock interaction patterns obtained in this study

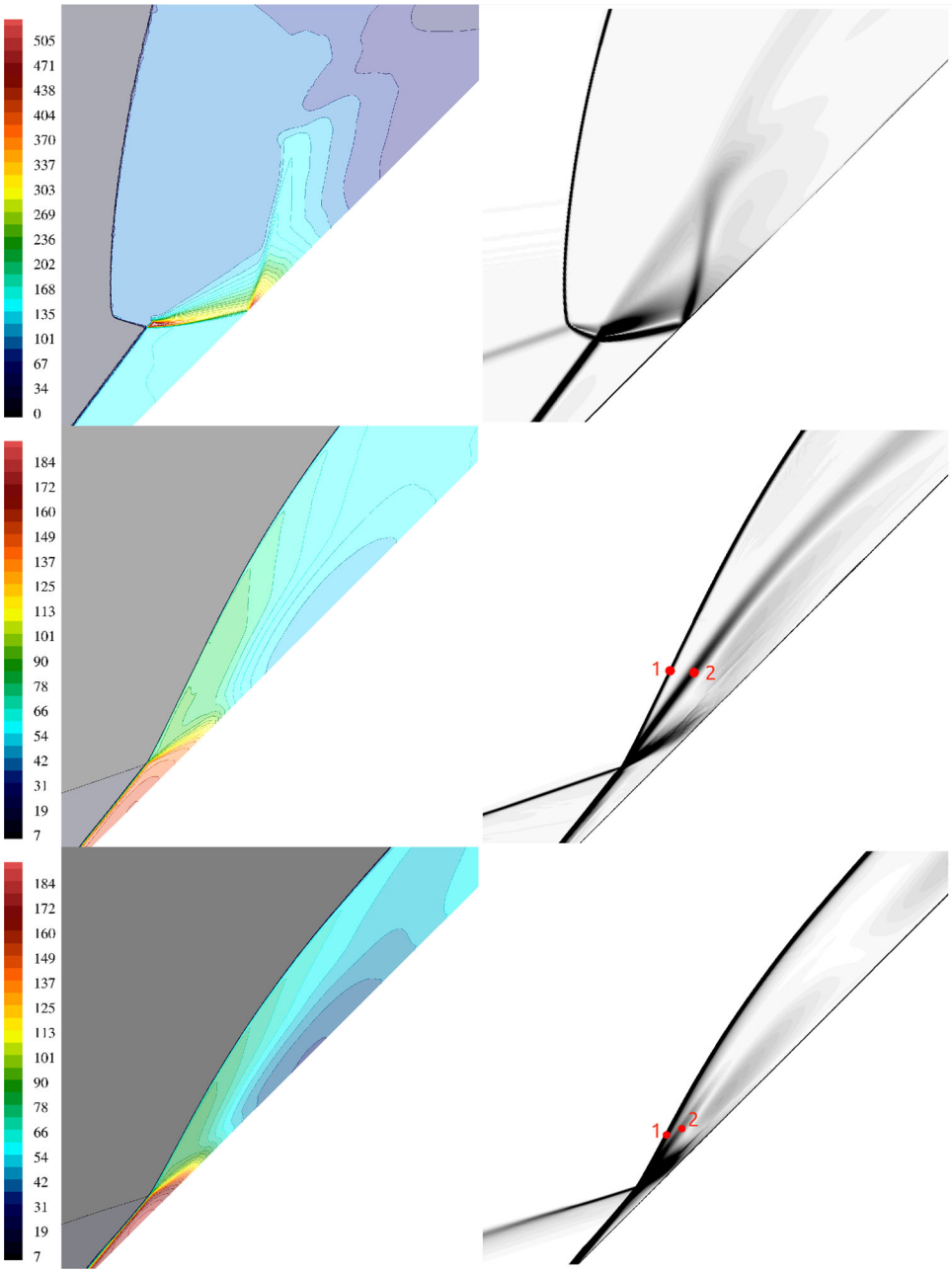

Fig. 7 CO_2–N_2 flow over 15°–45° double wedge. Normalized pressure p/p_∞ (left), numerical schlieren (right); from top to bottom: calorically perfect ideal gas, non-equilibrium with $T_\infty = 300$ K, $T_\infty = 1000$ K

non-equilibrium processes on the flow pressure behind the corner shock is discussed in the next section.

3.3 Non-equilibrium effects

Modelling the flow as a calorically perfect ideal gas does not account for chemical reactions and implies, among other things, that the energies associated with different molecular degrees of freedom are in equilibrium, and thus, only one temperature needs to be considered. However, in hypersonic conditions, thermal and chemical non-equilibrium effects play a significant role and cause the flow features to be significantly influenced by the values of freestream temperature, as shown in this study. With the increase in freestream temperature, the impact of non-equilibrium effects is more pronounced, as the shock interaction pattern differs from the one obtained with a calorically perfect ideal gas model. Overall, the flow becomes warmer, and a larger part of the energy that is transformed across a shock wave, from kinetic to internal, goes towards the excitation of the vibrational degrees of freedom of molecules, potentially up to the point of dissociation. As a result, when non-equilibrium effects are accounted for and as the freestream temperature increases, the shock waves become weaker (this is reflected in overall

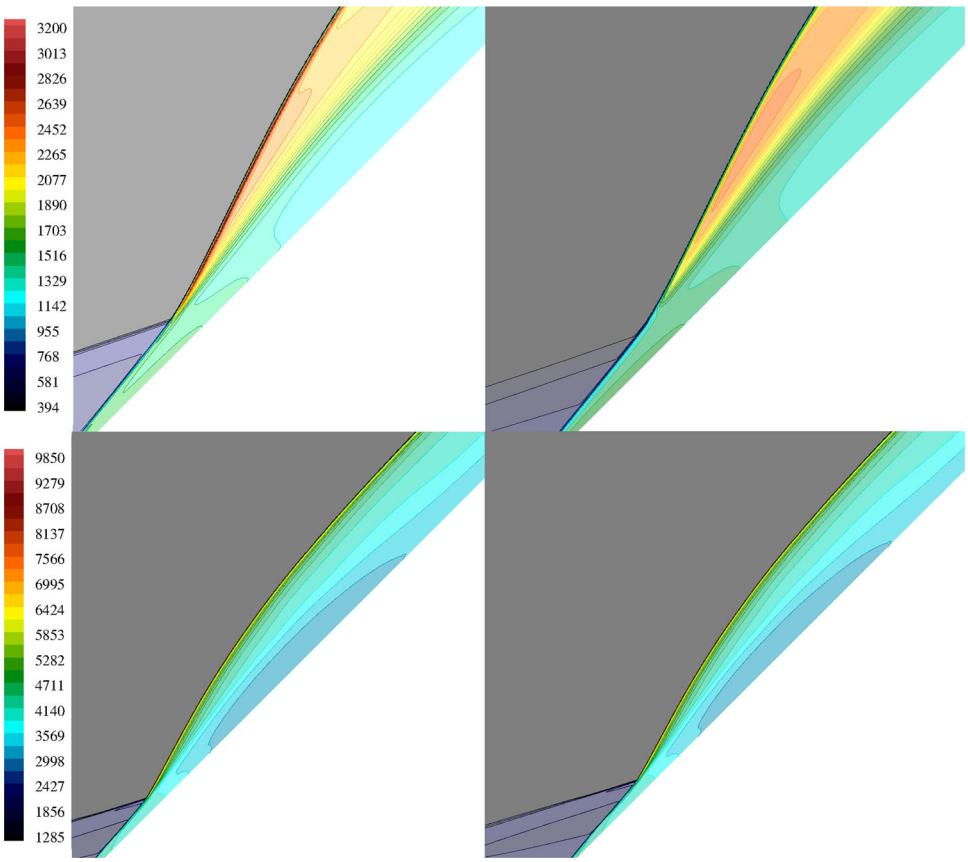

Fig. 8 CO_2–N_2 flow over 15°–45° double wedge. Translational temperature T_{tr} (left), vibrational temperature T_{ve} (right); from top to bottom: non-equilibrium with $T_\infty = 300$ K, $T_\infty = 1000$ K

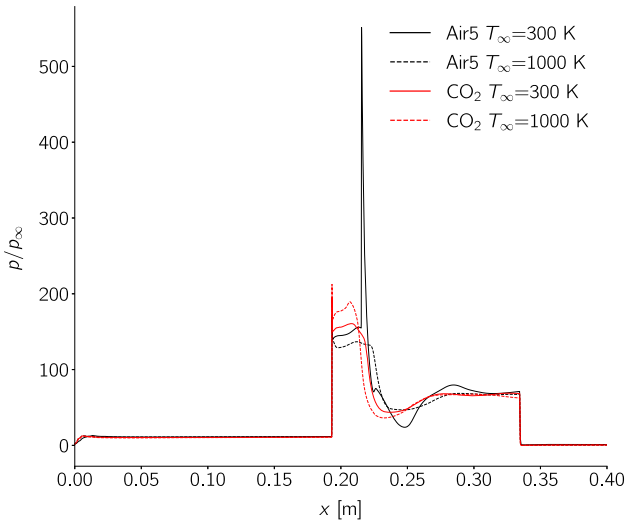

Fig. 9 Comparison of normalized surface pressure profile

smaller shock angles or length of normal shocks/Mach stems) despite the pattern observed and independently of the mixture in question. The results obtained numerically are consistent with this trend: for both air and CO_2–N_2 flows, for a higher freestream temperature, thermal non-equilibrium is stronger just behind the shocks (Figs. 5 and 8). However, vibrational relaxation is faster, which causes the flowfield to be, overall, closer to thermal equilibrium and the shocks to become weaker.

Nonetheless, the flow is also extremely sensitive to the atomic and molecular structure and characteristics of the mixture considered, and their impact on thermodynamic properties. Accordingly, for $T_\infty = 300$ K, the two mixtures result in completely different shock interaction patterns. For the case of air, looking at Fig. 5, it is interesting to notice that the shock interaction pattern changes significantly, as well as the degree of thermal non-equilibrium and the chemical activity (shown in Fig. 10). In contrast, the shock interaction patterns for the CO_2–N_2 flows do not change as much. The smaller impact of freestream temperature on the shock interaction patterns of a CO_2-dominated flow is consistent with the fact that the vibrational characteristic temperature of CO_2 is significantly lower than the one of N_2 and O_2 molecules of the air mixture; therefore, vibrational relaxation is much faster, and overall, the flow is prone to be closer to a state of equilibrium. For the higher value of freestream temperature, $T_\infty = 1000$ K, the two mixtures result in the same interaction pattern and very similar shapes. Both flows have a very thin layer (not visible in the case of CO_2–N_2) of strong thermal non-equilibrium behind the curved shock, but overall both flowfields are very close to thermal equilibrium.

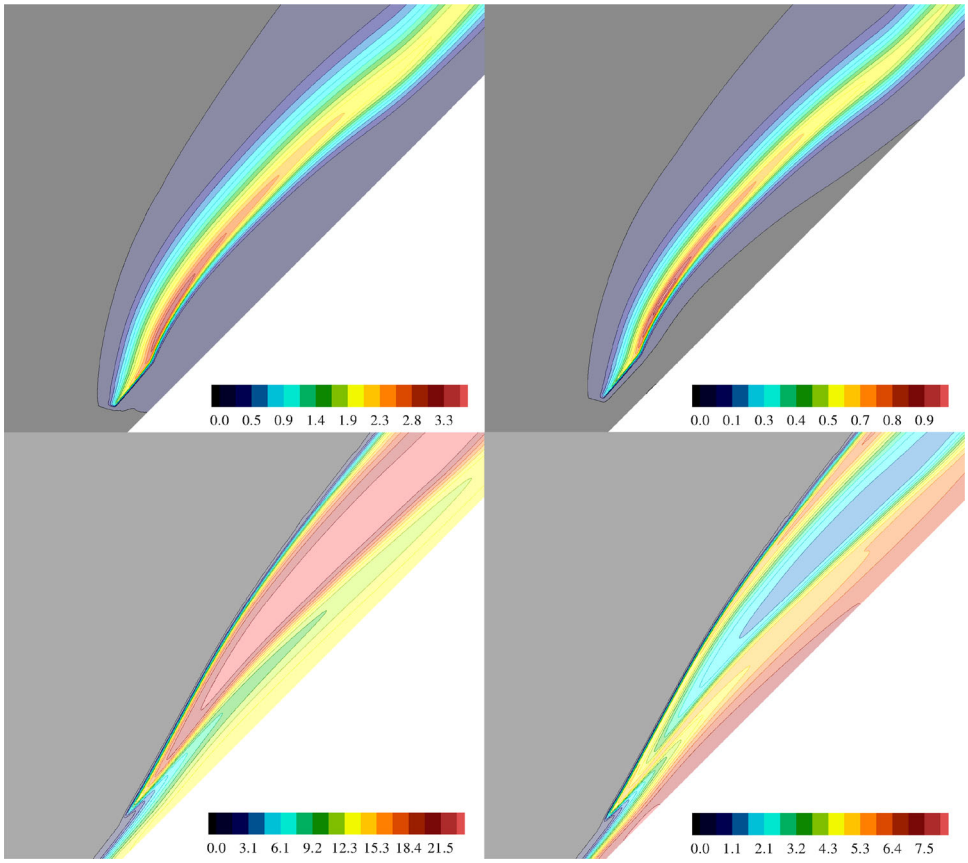

Fig. 10 Air flow over 15°–45° double wedge. Mass fractions for O (left) and NO (right); $T_\infty = 300$ K (top) and $T_\infty = 1000$ K (bottom)

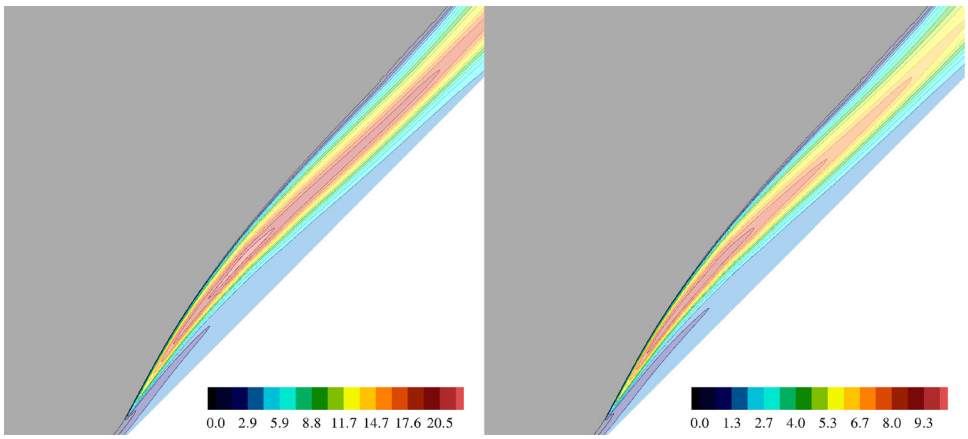

Fig. 11 CO_2–N_2 flow over 15°–45° double wedge. Mass fractions for CO (left) and O (right); $T_\infty = 1000$ K

Figure 10 shows the percentage mass fractions for O and NO species in the case of the air flow, test cases $T_\infty = 300$ K and $T_\infty = 1000$ K. Figure 11 shows the percentage mass fractions for CO and O species in the CO_2–N_2 flow, test case $T_\infty = 1000$ K. For the remaining test case, $T_\infty = 300$ K with the CO_2–N_2 mixture, no results are shown since the flow is frozen. For the case of air, as shown in Fig. 10, chemical activity is triggered for $T_\infty = 300$ K, with some O_2 and N_2 dissociation, and also NO formation, taking place. As the freestream temperature is increased to $T_\infty = 1000$ K, the occurrence of chemical reactions increases substantially—with the maximum mass fraction of O changing from 3.3% to 21.5%, and the maximum mass fraction of NO changing from 0.9% to 7.5%. For $T_\infty = 1000$ K, it can be observed that NO is almost non-existent in the regions where there is more atomic oxygen and that as it decreases from red to yellow regions in the figure, NO formation begins to occur (blue to orange to red regions). Figure 11 shows the percentage of mass fractions for CO and O species in the case of the CO_2–N_2 flow, test case $T_\infty = 1000$ K. Only at this value of freestream temperature, there seems to be enough energy to break the bonds of CO_2

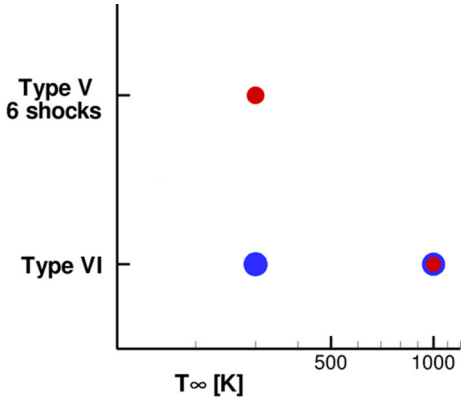

Fig. 12 Study of shock interaction patterns in air (red circles) and CO_2–N_2 (blue circles) flows, with respect to freestream temperature T_∞

molecules, resulting in a maximum mass fraction of 20.5% of CO and 9.3% of atomic oxygen. However, this energy is not sufficient to trigger CO dissociation, as there are no C atoms in the flowfield. Even though for the higher freestream temperature the shock waves for this mixture become weaker, the maximum pressure behind the oblique shock generated in the corner between the two wedges increases (Fig. 9). As dissociation starts to occur, the density jump across the oblique shock increases, and consequently, the pressure jump increases as well. For air, on the other hand, the shock pattern changes significantly, and the associated maximum pressure decreases considerably.

As explained in Sect. 2.1, a simple non-preferential dissociation model is employed to address the chemical–vibrational coupling. The latter model assumes that molecules can be dissociated from all vibrational states, which may be valid for situations where the freestream kinetic energy per unit mass is much larger than the dissociation energies of the molecules [21]. In preferential dissociation, on the other hand, it is considered that molecules dissociate more easily when vibrationally more excited. Molecules must "ladder climb" from lower to higher vibrational states to be dissociated. As a result, dissociation reactions are delayed, and vibrational temperature tends to be lower during the relaxation process, when compared to non-preferential dissociation [20]. It is likely that using a preferential dissociation model in this study would have had an impact on the results. It is assumed that less dissociation would occur and that, with lower vibrational temperatures, stronger thermal non-equilibrium would be obtained for each case. According to what is observed in this study, that would mean delaying the trend that has been shown as temperature rises. Further studies employing this model would be required to understand whether this would have a significant impact on the shape of the interactions patterns or even change them.

4 Conclusions

A numerical study was performed to understand how shock interference mechanisms in hypersonic flows change when a mixture other than air is considered. A Mach 9 flow over a 15°–45° double-wedge geometry was simulated for air and a CO_2–N_2 flow, and results were compared. Furthermore, to assess the influence of high-temperature effects for different conditions, a study of the shock interaction pattern was conducted with respect to two different values of the freestream temperature: $T_\infty = 300$ K and $T_\infty = 1000$ K. Figure 12 summarizes the results obtained in this study. It is shown that the freestream temperature has a greater impact on the shock interaction pattern in the flow of air than in CO_2-dominated flow. For different values of the freestream temperature, there is a great change in the wave structure for the flow of air, whereas for the CO_2–N_2 flow the change of pattern does not occur. It is overall observed that, due to the much faster vibrational relaxation of CO_2 molecules, the flows with a CO_2–N_2 mixture are closer to thermal equilibrium, and the patterns obtained are characterized by weaker shocks. However, at very high temperatures, thermal relaxation is fast in both mixtures and chemical reactions play a significant role. At a freestream temperature of 1000 K, the shock interaction pattern obtained is the same. Future work is looking into including viscous effects in the study, to understand how these patterns change when shock/boundary-layer interaction also plays a role. Employing a preferential dissociation model in this study and assessing its influence could also be considered.

Acknowledgements The authors wish to acknowledge the support of the EPSRC funded ARCHIE-WeSt High Performance Computer (www.archie-west.ac.uk), EPSRC Grant No. EP/K000586/1. The authors wish to thank K. Hanquist, from University of Arizona, for his contribution to the results obtained with the LeMANS code, presented in Sect. 2.3.

References

1. Edney, B.: Anomalous heat transfer and pressure distributions on blunt bodies at hypersonic speeds in the presence of an imping-

ing shock. Technical Report FFA-115, The Aeronautical Research Institute of Sweden (1968)
2. Olejniczak, J., Wright, M., Candler, G.: Numerical study of inviscid shock interactions on double-wedge geometries. J. Fluid Mech. **352**, 1–25 (1997). https://doi.org/10.1017/S0022112097007131
3. Halder, P., Sinhamahapatra, K.P., Singh, N.: Type-VI and type-V shock-shock interactions on double-wedge geometries using AUSM+ on unstructured grid. Int. J. Hypersonics **1**, 225–244 (2010). https://doi.org/10.1260/1759-3107.1.4.225
4. Hu, Z.M., Myong, R.S., Yang, Y.R., Cho, T.H.: Reconsideration of inviscid shock interactions and transition phenomena on double-wedge geometries in a $M_\infty = 9$ hypersonic flow. Theor. Comput. Fluid Dyn. **24**(6), 551–564 (2010). https://doi.org/10.1007/s00162-010-0188-4
5. Ben-Dor, G., Vasilev, E.I., Elperin, T., Zenovich, A.V.: Self-induced oscillations in the shock wave flow pattern formed in a stationary supersonic flow over a double wedge. Phys. Fluids **15**(12), L85–L88 (2003). https://doi.org/10.1063/1.1625646
6. Tchuen, G., Fogue, M., Burtschell, Y., Zeitoun, D., Ben-Dor, G.: Shock-on-shock interactions over double-wedges: comparison between inviscid, viscous and nonequilibrium hypersonic flow. In: Hannemann, K., Seiler, F. (eds.) 26th International Symposium on Shock Waves 1, pp. 1497–1502. Springer, Berlin (2009)
7. Tchuen, G., Burtschell, Y., Zeitoun, D.E.: Numerical study of the interaction of type IVr around a double-wedge in hypersonic flow. Comput. Fluids **50**(1), 147–154 (2011). https://doi.org/10.1016/j.compfluid.2011.07.002
8. Li, J., Zhu, Y., Luo, X.: Thermochemical non-equilibrium effects on type VI–V transition in hypersonic double-wedge flow. In: Bonazza, R., Ranjan, D. (eds.) 29th International Symposium on Shock Waves 1, pp. 167–172. Springer, Cham (2015)
9. Li, J., Zhu, Y., Luo, X.: On type VI–V transition in hypersonic double-wedge flows with thermo-chemical non-equilibrium effects. Phys. Fluids **26**(8), 086104 (2014). https://doi.org/10.1063/1.4892819
10. Hu, Z.M., Gao, Y.L., Myong, R.S., Dou, H.S., Khoo, B.C.: Geometric criterion for RR-MR transition in hypersonic double-wedge flows. Phys. Fluids **22**(1), 016101 (2010). https://doi.org/10.1063/1.3276907
11. Xiong, W., Zhu, Y., Luo, X.: On transition of type V interaction in double-wedge flow with non-equilibrium effects. Theor. Appl. Mech. Lett. **6**(6), 282–285 (2016). https://doi.org/10.1016/j.taml.2016.08.011
12. Xiong, W., Li, J., Zhu, Y., Luo, X.: RR-MR transition of a type V shock interaction in inviscid double-wedge flow with high-temperature gas effects. Shock Waves **28**(4), 751–763 (2018). https://doi.org/10.1007/s00193-017-0770-4
13. Atkins, C., Deiterding, R.: Modelling hypersonic flows in thermo-chemical nonequilibrium using adaptative mesh refinement. 7th European Conference on Computational Fluid Dynamics, Glasgow (2018)
14. Scoggins, J.B., Leroy, V., Bellas-Chatzigeorgis, G., Dias, B., Magin, T.E.: Mutation++: multicomponent thermodynamic and transport properties for IONized gases in C++. SoftwareX **12**, 100575 (2020). https://doi.org/10.1016/j.softx.2020.100575
15. Candler, G.: Computation of thermo-chemical nonequilibrium Martian atmospheric entry flows. 5th Joint Thermophysics and Heat Transfer Conference, Seattle, WA, AIAA Paper 1990-1695 (1990). https://doi.org/10.2514/6.1990-1695
16. Park, C., Howe, J.T., Jaffe, R.L., Candler, G.V.: Review of chemical-kinetic problems of future NASA missions, II: Mars entries. J. Thermophys. Heat Transfer **8**(1), 9–23 (1994). https://doi.org/10.2514/3.496
17. Armenise, I., Reynier, P., Kustova, E.: Advanced models for vibrational and chemical kinetics applied to Mars entry aerothermodynamics. J. Thermophys. Heat Transfer **30**(4), 705–720 (2016). https://doi.org/10.2514/1.T4708
18. Liao, D., Liu, S., Huang, J., Jian, H., Xie, A., Wang, Z.: Measurement and numerical simulation of shock standoff distances over hypersonic spheres in CO_2 in a ballistic range. Shock Waves **30**, 131–138 (2020). https://doi.org/10.1007/s00193-019-00923-1
19. Windisch, C., Reinartz, B.U., Müller, S.: Investigation of unsteady Edney type IV and VII shock-shock interactions. AIAA J. **54**(6), 1846–1861 (2016). https://doi.org/10.2514/1.J054298
20. Garbacz, C., Fossati, M., Maier, W., Alonso, J.J., Scoggins, J., Magin, T., Economon, T.D.: Numerical study of shock interference patterns for gas flows with thermal nonequilibrium and finite-rate chemistry. AIAA Scitech 2020 Forum, Orlando, FL, AIAA Paper 2020-1805 (2020). https://doi.org/10.2514/6.2020-1805
21. Gnoffo, P., Gupta, R., Shinn, J.: Conservation equations and physical models for hypersonic air flows in thermal and chemical nonequilibrium. NASA Technical Paper 2867, p. 158 (1989)
22. Park, C.: Assessment of two-temperature kinetic model for ionizing air. J. Thermophys. Heat Transfer **3**(3), 233–244 (1989). https://doi.org/10.2514/3.28771
23. Landau, L., Teller, E.: Systematics of vibrational relaxation. Phys. Z. Sowjetunion **10**, 34–38 (1936)
24. Millikan, R.C., White, D.R.: Systematics of vibrational relaxation. J. Chem. Phys. **39**(12), 3209–3213 (1963). https://doi.org/10.1063/1.1734182
25. Economon, T.D., Palacios, F., Copeland, S.R., Lukaczyk, T.W., Alonso, J.J.: Su2: an open-source suite for multiphysics simulation and design. AIAA J. **54**(3), 828–846 (2016). https://doi.org/10.2514/1.J053813
26. Palacios, F., Copeland, S., Lonkar, A., Alonso, J.: Adjoint-based goal-oriented mesh adaptation for nonequilibrium hypersonic flows. 51st AIAA Aerospace Sciences Meeting including the New Horizons Forum and Aerospace Exposition, Grapevine, TX, AIAA Paper 2013-0552 (2013). https://doi.org/10.2514/6.2013-552
27. Liou, M.S., Steffen, C.J.: A new flux splitting scheme. J. Comput. Phys. **107**(1), 23–39 (1993)
28. Park, C.: Review of chemical-kinetic problems of future NASA missions. I-Earth entries. J. Thermophys. Heat Transfer **7**(3), 385–398 (1993). https://doi.org/10.2514/3.431
29. Park, C., Jaffe, R.L., Partridge, H.: Chemical-kinetic parameters of hyperbolic earth entry. J. Thermophys. Heat Transfer **15**(1), 76–90 (2001). https://doi.org/10.2514/2.6582
30. Martin, A., Scalabrin, L., Boyd, I.: High performance modeling of atmospheric re-entry vehicles. J. Phys. Conf. Ser. **341**, 012002 (2012). https://doi.org/10.1088/1742-6596/341/1/012002